MOUNTAIN-PLAINS CONSORTIUM

MPC 24-552 | Y. Guo and B.J. Perry

DEVELOPMENT OF A NEW AIRBORNE PORTABLE SENSING SYSTEM TO INVESTIGATE BRIDGE RESPONSE

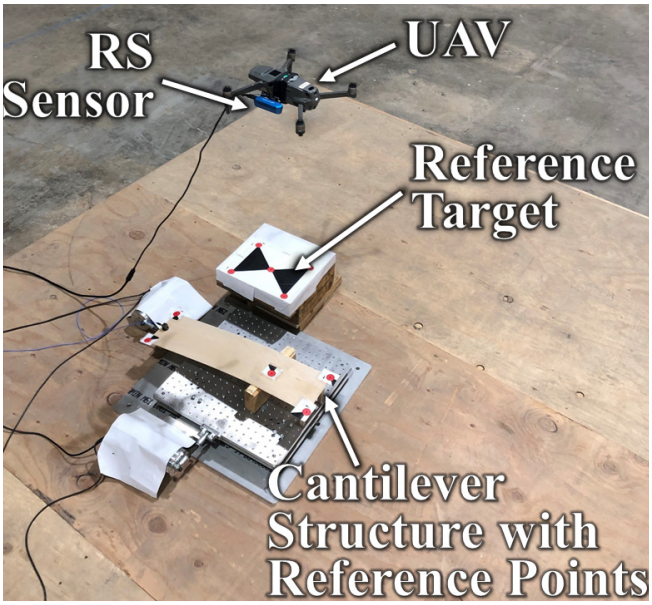

MOUNTAIN-PLAINS CONSORTIUM REGION 8

A University Transportation Center sponsored by the U.S. Department of Transportation serving the Mountain-Plains Region. Consortium members:

Colorado State University
North Dakota State University
South Dakota State University
University of Colorado Denver
University of Denver
University of Utah
Utah State University
University of Wyoming

Technical Report Documentation Page

1. Report No.	2. Government Accession No.	3. Recipient's Catalog No.
MPC-643		

4. Title and Subtitle	5. Report Date
Development of a New Airborne Portable Sensing System to Investigate Bridge Response	September 2024
	6. Performing Organization Code

7. Author(s)	8. Performing Organization Report No.
Yanlin Guo Brandon J. Perry	MPC 24-552

9. Performing Organization Name and Address	10. Work Unit No. (TRAIS)
Colorado State University Department of Civil and Environmental Engineering Fort Collins, CO 80523	11. Contract or Grant No.

12. Sponsoring Agency Name and Address	13. Type of Report and Period Covered
Mountain-Plains Consortium North Dakota State University PO Box 6050, Fargo, ND 58108	Final Report
	14. Sponsoring Agency Code

15. Supplementary Notes

Supported by a grant from the US DOT, University Transportation Centers Program

16. Abstract

This study proposes a new remote sensing technique to measure three-component (3C) dynamic displacement of three-dimensional (3D) structures. A sensing system with an unmanned aerial vehicle (UAV) platform and contact-free sensors (e.g., optical and infrared (IR) cameras) was employed to provide a portable and convenient alternative to conventional approaches that require sensor installation on a structure. The original contributions of this study include (1) integrating both optical and IR cameras with a UAV platform to measure dynamic structural response, and (2) developing new data post-processing algorithms (based on target identification, Direct Linear Transformation, and active stereo vision) to simultaneously extract the 3C displacement of a 3D structure from optical and IR videos, which presented a unique advantage compared to the existing UAV-based displacement measurement techniques that allow the measurements in only one or two directions using optical cameras or laser sensors. The efficacy of the proposed technique was validated through laboratory experiments.

17. Key Word	18. Distribution Statement
bridges, data collection, dislocation (geology), drones, infrared detectors, optical detectors, portable equipment, remote sensing, sensors, structural health monitoring	Public distribution

19. Security Classif. (of this report)	20. Security Classif. (of this page)	21. No. of Pages	22. Price
Unclassified	Unclassified	38	n/a

Form DOT F 1700.7 (8-72) Reproduction of completed page authorized

Development of a New Airborne Portable Sensing System to Investigate Bridge Response

Yanlin Guo, Ph.D. [1]
Brandon J. Perry [1]

[1] Department of Civil and Environmental Engineering
Colorado State University
Fort Collins, CO 80523

September 2024

Acknowledgments

This project is funded by Mountain-Plains Consortium (MPC) under grant number MPC-643. The opinions and findings of the authors do not necessarily reflect the view and opinions of MPC.

The work presented in this paper was conducted with support from Colorado State University (CSU) and the Mountain-Plains Consortium, a University Transportation Center funded by the U.S. Department of Transportation (FASTACT Grant No. 69A3551747108). The contents of this paper reflect the views of the authors, who are responsible for the facts and accuracy of the information presented. Additionally, the authors would like to acknowledge the CSU Drone Center and Mr. Christopher Robertson for providing the UAVs, support, and piloting expertise, and Prof. Francisco Ortega from the Department of Computer Science at CSU for providing the RS sensors.

Credit authorship contribution statement

Brandon J. Perry: Conceptualization, Investigation, Methodology, Software, Writing - original draft. **Yanlin Guo:** Conceptualization, Methodology, Writing - reviewing and editing, Supervision, Funding acquisition.

Declaration of competing interest

The authors declare that they have no known competing financial interests or personal relationships that could have appeared to influence the work reported in this paper.

Disclaimer

The contents of this report reflect the views of the authors, who are responsible for the facts and the accuracy of the information presented. This document is disseminated under the sponsorship of the Department of Transportation, University Transportation Centers Program, in the interest of information exchange. The U.S. Government assumes no liability for the contents or use thereof.

ABSTRACT [1]

This study proposes a new remote sensing technique to measure three-component (3C) dynamic displacement of three-dimensional (3D) structures. A sensing system with an unmanned aerial vehicle (UAV) platform and contact-free sensors (e.g., optical and infrared (IR) cameras) was employed to provide a portable and convenient alternative to conventional approaches that require sensor installation on a structure. The original contributions of this study include (1) integrating both optical and IR cameras with a UAV platform to measure dynamic structural response, and (2) developing new data post-processing algorithms (based on target identification, Direct Linear Transformation, and active stereo vision) to simultaneously extract the 3C displacement of a 3D structure from optical and IR videos, which presented a unique advantage compared to the existing UAV-based displacement measurement techniques that allow the measurements in only one or two directions using optical cameras or laser sensors. The efficacy of the proposed technique was validated through laboratory experiments.

[1] This report is based on the contents from the following published journal paper:
Perry, B.J., and Guo, Y. (2021), "A portable three-component displacement measurement technique using an unmanned aerial vehicle (UAV) and computer vision: a proof of concept", Measurement, 176, 109222.

TABLE OF CONTENTS

1. INTRODUCTION **1**
2. METHODOLOGY **4**
2.1 2C Planar Measurement 4
2.2 1C Depth Measurement 8
3. EXPERIMENTAL TESTING **10**
3.1 Description of Data Sets 10
3.2 Preliminary Experimental Analyses on 2C and 1C Measurements 11
3.2.1 Analysis of 2C Planar Measurement 11
3.2.2 Analysis of 1C Depth Measurements 13
3.3 Proof of Concept: An Experiment on 3C Measurement 16
4. DISCUSSION **22**
5. CONCLUDING REMARKS **25**
REFERENCES **26**

LIST OF TABLES

Table 2.1 Camera parameters 6
Table 3.1 Results from 2C non-stationary planar validation test 12
Table 3.2 Results of stationary 1C RS depth sensor 14
Table 3.3 Results from 1C non-stationary depth validation test 16
Table 3.4 Results from 3C measurement experiment using a UAV equipped with an RS sensor 19
Table 3.5 Comparison of proposed technique to other literature references 21
Table 3.6 Camera configuration for scaling-up the proposed technique 21
Table 4.1 Price estimations (prices in USD) 24

LIST OF FIGURES

Figure 2.1 Proposed methodology overview 4
Figure 2.2 Concept of 2C planar measurement 6
Figure 2.3 Reference target diagram 7
Figure 2.4 Concept of 1C depth measurement 8
Figure 2.5 Camera calibration results of the RS optical camera 9
Figure 3.1 Overview of non-stationary 2C planar measurement set-up 10
Figure 3.2 Sample displacement measurement results from non-stationary sensor 11
Figure 3.3 Set-up of stationary 1C validation test 13
Figure 3.4 Sample displacement measurement results from stationary 1C RS 14
Figure 3.5 Noise floor of the RS depth sensor 15
Figure 3.6 Sample displacement measurement results from non-stationary RS depth sensor 15
Figure 3.7 POV of RS sensors from 0.75m 16
Figure 3.8 Set-up of 3C measurement experiment using a UAV 18
Figure 3.9 Displacement in *x*- and *y*-directions measured by UAV. 18
Figure 3.10 Displacement in *z*-direction measured by UAV. 19
Figure 3.11 Wavelet analysis of *z*-direction displacement 20
Figure 3.12 Horizontal Measuring Distance (HMD) with *Stable* and *Extreme* drift over two-lane bridge 20

EXECUTIVE SUMMARY

This study proposes to instrument an unmanned aerial vehicle (UAV) with integrated optical and infrared (IR) sensors, through which the video of two-component (2C) planar movement is captured by the optical sensor, and, simultaneously, the one-component (1C) depth movement is recorded by the IR sensors in conjunction with an IR projector (e.g., active stereo vision). A double-faceted computer vision technique was developed to take measurements from the recorded image frames. The major contribution of the study was to allow the measurement of all three-component (3C) dynamic displacements, which currently lacked UAV-enabled sensing. Note that although UAVs can hover in the air stably and allow for high-quality image capturing and robust target identification, there is slight drifting of the UAV (up to ±0.5-m in the three directions), which may introduce significant errors in dynamically sensitive applications (e.g., dynamic displacement measurement), due to the UAV's movement being added to the measurements. To eliminate the errors due to the UAV's movement, the UAV must be self-aware (e.g., know the small, random drifts of the UAV itself as it is hovering in the air) in all three directions. This 3C self-awareness of the UAV was achieved by measuring the relative displacements of UAV with respect to stationary reference targets. Then, the motion of the UAV can be removed from the measurements. To prove the concept of the proposed technique, an Intel Realsense D435 (RS), with integrated IR sensors, projector, and optical RGB camera, was equipped on a DJI Mavic 2 Pro for experimental testing. The IR sensor provided the ability to quickly test a proof of concept of the proposed technique.

In this report, the methodology of the proposed technique is introduced first. Then, experimental results are shown to demonstrate its efficacy. The maximum frequency and damping estimation errors in the experiments were 3.5% and 4.4%, respectively, and the root-mean-square error (RMSE) was less than 2-mm, proving that the measurement accuracy achieved by the proposed technique is sufficient for structural health monitoring application to civil structures. Also, a detailed discussion is presented outlining the unique advantages of the proposed technique, its limits, and its scalability. Finally, the concluding remarks are presented.

1. INTRODUCTION

Understanding the dynamics of structures is critical for evaluating long-term structural performance and decision-making regarding maintenance and operation of the structure. Quantifying the displacement of structural vibration is an important means to evaluate the dynamic performance of structures under various dynamic loading, such as winds, traffic, impact loading, etc. Once the three-component (3C) dynamic displacement of structures is measured, system identification methods can be applied to estimate the dynamic properties of the structure. If the time series is stationary, the conventional system identification (SI) methods (e.g., random decrement technique, frequency domain decomposition, stochastic subset identification) can be used [1], [2], [3], [4]. On the other hand, if the time series are non-stationary, more advanced SI techniques (e.g., time–frequency domain approaches) can be used [5], [6], [7]. Additionally, the 3C displacement measurements can also be useful for the development of various data-driven approaches for structural health monitoring (SHM) [8], [9], [10], [11], [12].

Traditionally, accelerometers are the most commonly used sensors to measure the dynamic response of structures [13], [14], [15], [16]. For instance, Linderman et al. attached 26 accelerometers on the I-35W Saint Anthony Falls Bridge in Minneapolis, Minnesota, to measure the dynamic response of the structure[17]. Although the accelerometers provided a wealth of information on dynamic characteristics of large-scale bridges, the total displacements could not be fully recovered due to the inability to solve for the constants of integration when double integrating the accelerations, leading to the loss of background movement of structural response due to winds[18]. To rectify the lack of direct displacement measurements, Global Positioning Systems (GPS) were implemented for dynamics monitoring[14], [15]. These conventional contact sensor-based monitoring systems require sensors placed at multiple locations, and their instrumentation on large-scale structures may impose logistical challenges for the structure owners and researchers[17], [19]. For example, careful pre-planning of the sensor placement and management of the wires is needed for a wired system, while the challenges of synchronization of the sensors and risk of lost communication must be properly handled for a wireless system[17].

Consequently, the contact sensors might not be easily relocated after installation. Recently, stationary, non-contact remote sensing systems using cameras or laser Doppler have been deployed to measure displacement[20], [21], [22], [23], [24], [25], [26], [27], [28], [29], [30], [31]. With these stationary systems, highly accurate measurements are possible using either a painted speckle pattern on the structure or reference markers; however, finding a safe placement area for the stationary system might be difficult in some applications. In this context, this study intended to develop a portable, UAV-enabled dynamic measurement technique that can be easily applied to different structures, as a more convenient alternative to contact sensory or stationary non-contact sensor-based systems for short-term dynamic monitoring and modal testing.

Recently, unmanned aerial vehicles (UAVs) have been deployed to assist bridge inspectors and managers. UAV-enabled sensors have the potential to provide information from various difficult-to-access locations of a bridge on a faster, more cost-effective and safer platform when compared to traditional techniques. Some studies have already explored the potential of utilizing UAVs as a non-destructive testing technique to assist in bridge inspection by identifying the surface and/or subsurface defects of structures[32], [33], [34], [35]. Some research on using optical sensors on UAVs tracks the displacements of a structure in either the two-component (2C) planar directions (the plane perpendicular to the camera) or the one-component (1C) depth direction (the out-of-plane direction or the distance from the camera to the structure). With the assumption that the out-of-plane displacement of civil infrastructure is minimal, 2C planar displacements of structures can be measured with optical sensors on UAVs[36], [37]. Hoskere et al. used high-pass filtering to remove noise imposed by the UAV's drift, and a scale-factor was calculated to relate real-world measurements to pixels to measure 2C planar displacement[36]. Kalaitzakis et al.

implemented a painted speckle pattern on a concrete beam to measure the strain during a four-point loading test with an additional painted speckle pattern on a stationary reference[37].

Other studies can measure the out-of-plane displacement of structures[38], [39], [40]. Garg et al. used a laser Doppler vibrometer, which accurately measures the reflection of a high-frequency wave, to calculate the out-of-plane displacement of an object[38], [39]. Catt et al. implemented passive stereo vision by mounting two cameras at a known distance apart to measure the out-of-plane deformations of a deformable board with a random speckle pattern[40]. The proposed algorithm processed the speckled pattern placed on the board to measure the 1C depth; however, the drift of the UAV was not compensated resulting in the 2C displacement of the deformable board not being realized. Although aforementioned techniques using painted speckle pattern can provide accurate measurements within the speckled area (such as[40] or[37]), they do not take advantage of the entire field of view (FOV) of the camera, and implementing these techniques in the real-world may be challenging due to the large-scale of the structures and workforce required to install the detailed patterns.

Yoon et al. proposed a 2C planar UAV-enabled measurement methodology without a speckle pattern by identifying, matching, and tracking feature points in the background of the video to estimate the camera's pose and recover the 3C translation and rotation of the UAV; however, the proof of concept still required LED lights as targets[41]. UAVs have also been used to identify the vibration modes of a structure without correcting for the movement of the UAV[42]. The existing studies have not attempted to measure the full 3C displacements of a structure using UAV-enabled sensors without the aid of a painted speckle pattern, which can be critical for certain types of structures, such as long-span bridges and cables.

As the capabilities of various sensors improve, a more diverse application of sensors on UAVs becomes possible. Recently, several sensing products, which employ active stereo vision to measure depth using infrared (IR) structured light (or a virtual speckle pattern) with IR cameras (as opposed to a real speckle pattern used in the previous studies), have made an appearance on the marketplace. Apple's FaceID, Intel's RealSense Depth Camera and Microsoft's Kinects sensor are two examples. As an alternative to active stereo vision, passive stereo vision uses two optical cameras to measure the depth using feature-based matching[43], [44], [45]. For both types of approaches, the operating distance between the sensor and the object depends on a camera's configuration (e.g., focal length, resolution, and baseline between two cameras). The active stereo vision is suitable for dark or unlit environments (e.g., indoor under any lighting condition or outdoor under shade or after sunset), while the passive stereo vision is appropriate for well-lit environments (e.g., under direct sunshine or indoor with good lightening). Active stereo vision takes depth measurements on the matched virtual speckles; thus, it works well regardless of surface texture.

On the other hand, the passive stereo vision can take depth measurements on either matched keypoints from natural features or matched patterns of painted speckle or markers. When applying passive stereo vision to displacement (or strain) measurements on non-textured surfaces (e.g., concrete), painted speckle or markers are typically required[44], [46], because the density of keypoints found from natural features is too low to provide the desired resolution in a depth map. The active stereo vision is more advantageous than the passive stereo vision for achieving high-resolution depth measurements without requiring painted patterns or a highly textured surface; therefore, it is more attractive for applications on many civil structures, as long as the working environment is not under direct sunlight.

Other alternative active sensors for depth measurement include laser scanners, such as Light Detection and Ranging (LiDAR) and Laser Doppler Vibrometer. LiDAR has been used with UAV platforms to measure full-field depth for survey purposes[47], but they are not applicable for dynamic measurements. A Laser Doppler Vibrometer has been used on a UAV platform to measure the dynamic displacement[38], [39], but it only measures a single location during each test. Thus, the active stereo

vision might be more advantageous than a laser sensor in terms of allowing a full-field dynamic measurement.

Considering the advantages and shortcomings of the aforementioned techniques, this study proposed instrumenting a UAV with integrated optical and IR sensors, through which the video of 2C planar movement is captured by the optical sensor, and simultaneously the 1C depth movement is recorded by the IR sensors in conjunction with an IR projector (e.g., active stereo vision). A double-faceted computer vision technique is developed to take the measurements from the recorded image frames. The major contribution of the study is to allow the measurement of all 3C dynamic displacements, which is currently lacking in UAV-enabled sensing. Note that although UAVs can hover in the air stably and allow for high-quality image capturing and robust target identification, there is slight drifting of the UAV (up to ±0.5-m in the three directions), which may introduce significant errors in dynamically sensitive applications (e.g., dynamic displacement measurement), due to the UAV's movement being added to the measurements. To eliminate the errors due to the UAV's movement, the UAV must be self-aware (e.g., know the small, random drifts of the UAV itself as it is hovering in the air) in all three directions. This 3C self-awareness of the UAV was achieved by measuring the relative displacements of UAV with respect to stationary reference targets. Then the motion of the UAV could be removed from the measurements.

To prove the concept of the proposed technique, an Intel Realsense D435 (RS), with integrated IR sensors, projector, and optical RGB camera, was equipped on a DJI Mavic 2 Pro for experimental testing. The RS sensor was originally developed for human–computer interactions, where it is used to measure a relative location of hand movements using active stereo vision[48]. Although dynamic structural measurements are not the RS sensor's intended use, it has shown great success in various applications, such as measuring human heart rate and estimating fill volume of containers[49], [50]. This self-contained sensor provides the ability to quickly test a proof of concept of the proposed technique.

In the following sections, methodology of the proposed technique is introduced first. Then, experimental results are shown to demonstrate its efficacy. The maximum frequency and damping estimation errors in the experiments are 3.5% and 4.4%, respectively, and the root-mean-square error (RMSE) is less than 2-mm, proving the measurement accuracy achieved by the proposed technique is sufficient for SHM application to civil structures (typically an error of few percent in the frequency and below 10%–15% error in damping estimation are expected[4]). Also, a detailed discussion is presented, outlining the unique advantages of the proposed technique, its limits, and its scalability.

2. METHODOLOGY

The computer vision algorithms of the proposed double-faceted 3C displacement measurement technique is introduced in this section. An initial overview of the workflow is presented in Figure 2.1.

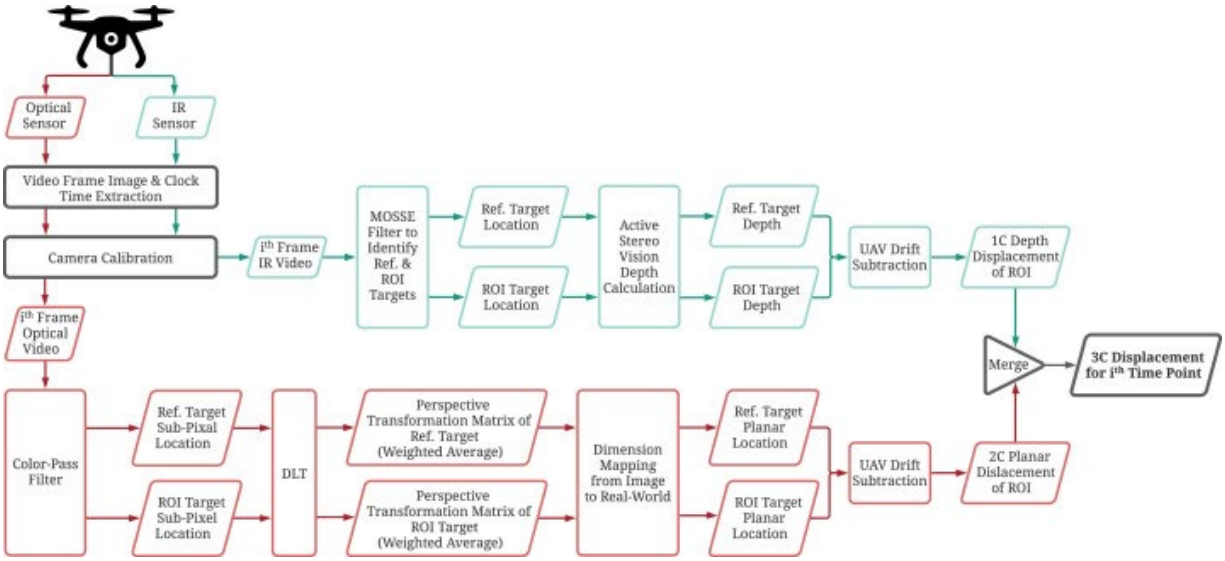

Figure 2.1 Proposed methodology overview

2.1 2C Planar Measurement

To measure the 2C planar movement of the ROI, first, the camera must be calibrated to ensure the physical dimensions measured by the cameras are free of tangential and radial distortion errors caused by the lens. Camera distortion correction is a well-studied problem within the computer vision field[51], [52], [53], [54], [55] and many off-the-shelf software and toolboxes are available. In this study, both a proprietary calibration software developed specifically for the RS optical and IR sensors included in the Realsense SDK 2.0 and an open-source MATLAB camera calibration toolbox[56] were tested. A grid pattern target and a total of 14 pictures were used in the calibration. Both tools achieved similar performance. In the following displacement measurement study, only the calibration results using Realsense SDK 2.0 were used. Once the camera is calibrated, it can be used for multiple surveys; however, if the camera is jarred hard enough, so some structural components of the lens or camera are moved or affected, the camera must be re-calibrated. Also note that changing temperatures can cause errors in the camera calibration[57]. For instance, heating and cooling the camera by 10°C can cause up to a pixel drift with larger pixel drift from larger temperature changes; therefore, it is recommended the camera stays at a relatively constant temperature after calibration or re-calibration is needed.

With the calibrated sensors, the UAV hovers next to a structure or object and the optical sensor records a video of the object moving in the *x*-*y* plane (Figure 2.2). In this study, the optical sensor inside the RS sensor was used. This optical (or RGB) sensor is a 2.729×1.550-mm Complementary Metal Oxide Semiconductor (CMOS) sensor with a rolling shutter capable of capturing 1920×1080-pixel at 30-fps (or a faster sampling frequency at a lower resolution), and a 1.93-mm focal length; the horizontal angular FOV of the camera is 69.4 (Table 2.1). The camera attached to a hovering UAV captured image frames that contained the targets of both the ROI on the vibrating object (e.g., a bridge under traffic–induced excitation) and that of the stationary reference target (Figure2.2). The maximum distance between

stationary reference and the moving object that allows both in the same frame is dictated by the FOV of the optical camera, the UAV flight height, and the level of UAV horizontal drift. The UAV flight height is controlled by the desired level of accuracy for depth measurement, which will be discussed in Section2.2, while the drift of UAV is dependent on a particular UAV system and wind conditions. The motion of the UAV was recovered by tracking the relative movement of the stationary reference target with respect to the UAV; while the relative motion between the UAV and the ROI was extracted by tracking the movement of the ROI. By adding the movement of the ROI with respect to the UAV, X_{ROI}, to the movement of the UAV with respect to the ground, X_{UAV}, the true movement of the ROI, X_{True}, was found, as shown in Eq.(1).

$$X_{True}=X_{ROI}+X_{UAV} \quad (1)$$

A robust target identification algorithm was developed to simultaneously track the targets on the ROI and those on the stationary reference target. To promote the fast and simple implementation of the proposed framework, a color detection-based technique was developed to robustly and accurately find the center points of the red-circle-target (Figure 2.3a) used in the experiments. The red-circle-target also provided a scale to help accurately transform the image coordinates into real-world coordinates in the next step. Note that it is not necessary to use this specific type of reference target; only measurable target and identifiable reference points are needed. The idea of this approach was to first detect the target using its color (red in this case). To accomplish this, the image was converted from RGB to a Hue, Saturation, Value (HSV) color model. The Hue represents the specific color value ranging from 0–255, with 0, 85, 170 representing red, green, and blue, respectively, while the Saturation and Value represent how close the color is to black or white. Using the HSV color model is more advantageous for color identification in the images compared to using an RGB color model, because only one value (versus the three values in the RGB model), e.g., the Hue value, represents the color present. Moreover, since the reference target is on a white background (Figure 2.3a), the red color is filtered easily using a small range of Hue values that encompasses the scale points on the reference. Since certain Hue values are the only color allowed to pass, the filter is called a *color-pass filter*. The color-pass filter results in the binary image shown in Figure 2.3b. Then, the contours in the binary image are found by a contours detector developed in [58]. The center is estimated by taking an average of the pixel locations inside the contour. Knowing the general location of each reference point in the image (e.g., upper left corner, bottom right corner, etc.), a search was performed in each quadrant of the image to distinguish the different reference points. The result is shown in Figure 2.3c. The major advantages of the proposed color-pass filter include (1) it provides subpixel detection accuracy and (2) it is more computationally efficient over other target detectors, such as template matching that requires a reference image and an exhaustive search and Hough Transforms that needs additional higher-level processing. The proposed color-pass filter technique is generalizable for the field application when applied in conjunction with other object tracking techniques. For example, one may first use an object tracker, such as the MOSSE filter[59] or CRST[60] to track the general location of the target. Then, the background is masked out and the color-pass filter is applied onto the masked image to detect the reference points with high accuracy. Note that when used solely, object trackers like MOSSE filter do not provide the subpixel accuracy needed for displacement measurements[61], which highlighted the value of the proposed color-pass filter.

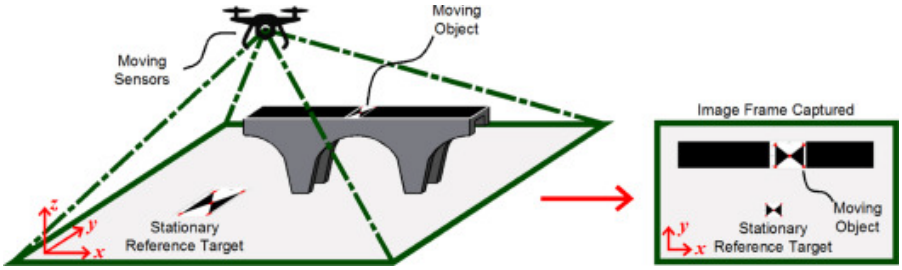

Figure 2.2 Concept of 2C planar measurement

Table 2.1 Camera parameters

Empty Cell	**Sensor type**	**Sensor dimensions (mm)**	**Shutter**	**Focal length (mm)**	**Horizontal FOV (deg.)**	**Video resolution (pixel × pixel × fps)**
RealSense optical	CMOS	2.729×1.550	Rolling	1.93	69.4	1280×800×30
						848×480×90
						840×100×100
RealSense infrared	CMOS	3.90×2.45	Global	1.93	86.0	1920×1080×30
						960×540×60

After the reference target is successfully found, the actual amplitude of the displacement must be recovered by mapping the pixels on image to the real-world dimensions through a direct linear transformation (DLT). The DLT ensures (1) image warping due to non-perpendicular camera angles is eliminated to enhance measurement accuracy in the plane, and (2) each pixel is scaled to a real-world dimension (e.g., in millimeter). Item (1) is needed to ensure there is no warping of the image. In the real-world application, the video can be captured at a nearly perpendicular angle; however, small misalignment typically exists due to the random drifts of the UAV. The DLT corrects the image for non-perpendicular (e.g., the small misalignment) and skewed camera angles to achieve a high measurement accuracy. On the other hand, item (2) allows real world measurements to be taken directly from the image. To begin the DLT, the relationship (or perspective transformation matrix) between a known reference point in the real-world in space coordinates, $X=[X,Y,1]^T$, and its location in pixel points in image coordinates, $x=[x,y,1]^T$, must be known. Note the image observation points (x,y) were obtained from the pre-processed image with radial and tangential distortions corrected in the camera calibration process. By knowing both image and space coordinates, the DLT is implemented to solve for the perspective transformation matrix, A, with respect to the linear system,

$$X \sim Ax \qquad (2)$$

where ~ denotes equality up to a scale. The resulting A is used to transform every pixel of the image by the following,

$$P_{DLT}(X,Y) = P_{Original}\left(\frac{A_{11}x + A_{12}y + A_{13}}{A_{31}x + A_{32}y + A_{33}}, \frac{A_{21}x + A_{22}y + A_{23}}{A_{31}x + A_{32}y + A_{33}}\right) \qquad (3)$$

where , $P_{DLT}(X,Y)$ is the transformed image with real-world coordinates at X and Y and $P_{Original}(x,y)$ is the original image in image coordinates. As a note, the transformation is only viable on the z-direction plane where the reference targets are placed; if the z displacement (the distance from the camera to the ROI) is significant, errors can occur in the measurement. Therefore, for the most accurate measurements, it is best that DLT is performed on a frame-to-frame basis to eliminate the impact due to camera displacement in z-direction. However, updating the perspective transformation matrix, A, with every frame introduces noise in the measured signal due to the subpixel location errors of the reference points. To reduce this noise, it is recommended to take a weighted average of A, for each frame of the video with,

$$A_i^* = \eta A_i + (1-\eta) A_{i-1} \quad (4)$$

where, A_i^* is the perspective transformation matrix used in the DLT for the i th frame, A_i is the calculated perspective transformation matrix of the ith frame, and A_{i-1} is the previous perspective transformation matrix. Through testing, it was found that η=0.125 produced smooth and accurate results shown in Section 3. After raw images are transformed through the process of camera calibration and DLT, the distances between points on the image represent the real-world dimensions, and the amplitude of the displacement in the real-world is finally recovered. One should note that the DLT is sensitive to the exact subpixel location used for scaling. Therefore, it is important to ensure each subpixel location extracted from the image corresponds to the exact location of the reference point on the real-world scale for accurate measurements. As previously mentioned, the color-pass filter developed in this study robustly identified the subpixel locations in the image.

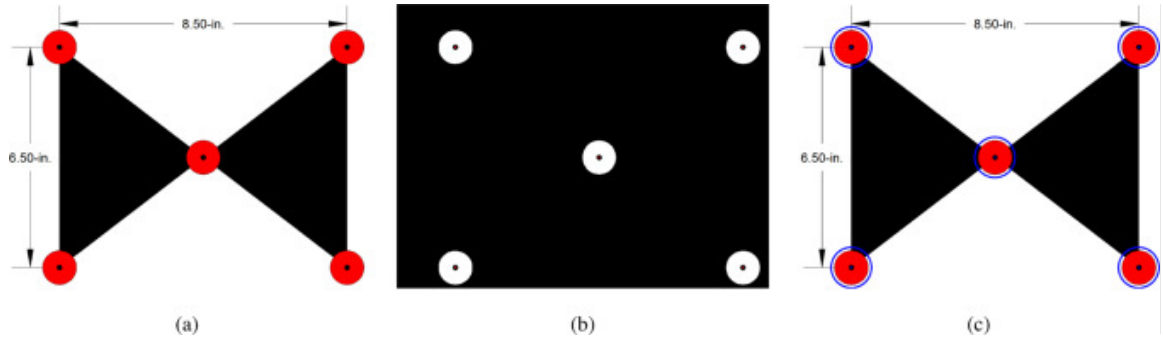

Figure 2.3 Reference target: (a) Reference and red scale point used, (b) Red-Pass color filter of target, and (c) Identified red target. (For interpretation of the references to color in this figure legend, the reader is referred to the web version of this article.)

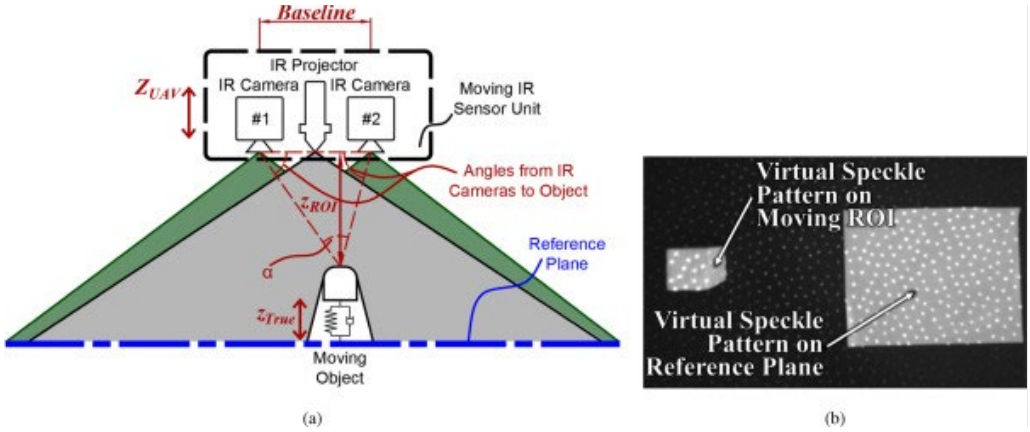

Figure 2.4 Concept of 1C depth measurement: (a) Schematic plot and (b) View of virtual speckle pattern from RS IR camera

2.2 1C Depth Measurement

The 1C depth measurement is also realized by the RS sensor set. Similar to the 2C measurement facet discussed in the previous section (Figure 2.1)

The RS depth sensor used in this study had a 360-mW average IR laser projector with a nominal wavelength of 850-nm ± 10-nm. This projector emits a virtual speckle pattern, which is not visible with the human eye, onto the FOV of the camera. Two IR 3.90×2.45-mm CMOS sensors with a global shutter and wavelength range of 400–865-nm were also included in this sensor set. Each IR camera can capture video at 1280×720-pixel at 30-fps (or a faster sampling frequency at a lower resolution) and 1.93-mm focal length; the horizontal FOV of the sensor is 86.0° (Table 2.1)accurate measurements; the baseline for the RGB sensor and IR projector are also known. A schematic of the sensor set-up is shown in Figure 2.4a. By projecting a seemingly random but known IR speckle pattern onto the objects (Figure 2.4b), each speckle was matched between the two IR cameras. With the matched speckles and a known baseline between the two IR cameras, the angle from each camera to the speckle was calculated and the distance from the speckle to the camera was found. Using active stereo vision, every available pixel in the image was transformed to the depth measurements in real-time and the depth from the RS sensor to the ROI was found. This calculation is embedded onboard the RS sensor.

Since the IR projector covered the entire FOV of the camera, the depth throughout the entire image was solved, allowing the full-field displacement measurement. To enhance the measurement accuracy and reduce depth measurement noise, a small area of pixels (within a one cm^2 range) on the ROI can be selected, averaged, and considered as a point to represent the ROI. Since both the object and the UAV are moving in the two horizontal directions (x- and y-directions), the ROI and the stationary reference must also be tracked in the IR video to allow for the same point measurement. To accomplish this, a MOSSE filter[59] was used to track the areas of interest in the x- and y-directions. Although a MOSSE filter is not recommended to be used solely in the 2C planar measurement due to the lack of subpixel precision, it was admissible for the 1C depth measurement, since the average depth for speckle points in a small area was taken. As a note, shadow effects of the IR projector or cameras may limit the performance of full-field measurement, which is a common drawback to stereo vision; measuring the displacement from the top surface of a structure, as in this study, alleviates this issue. Using this approach, the relative dynamic displacements between the UAV and the object, and that between the UAV and the reference plane were measured. Then, the true motion of the object was extracted by removing the motion of the UAV itself.

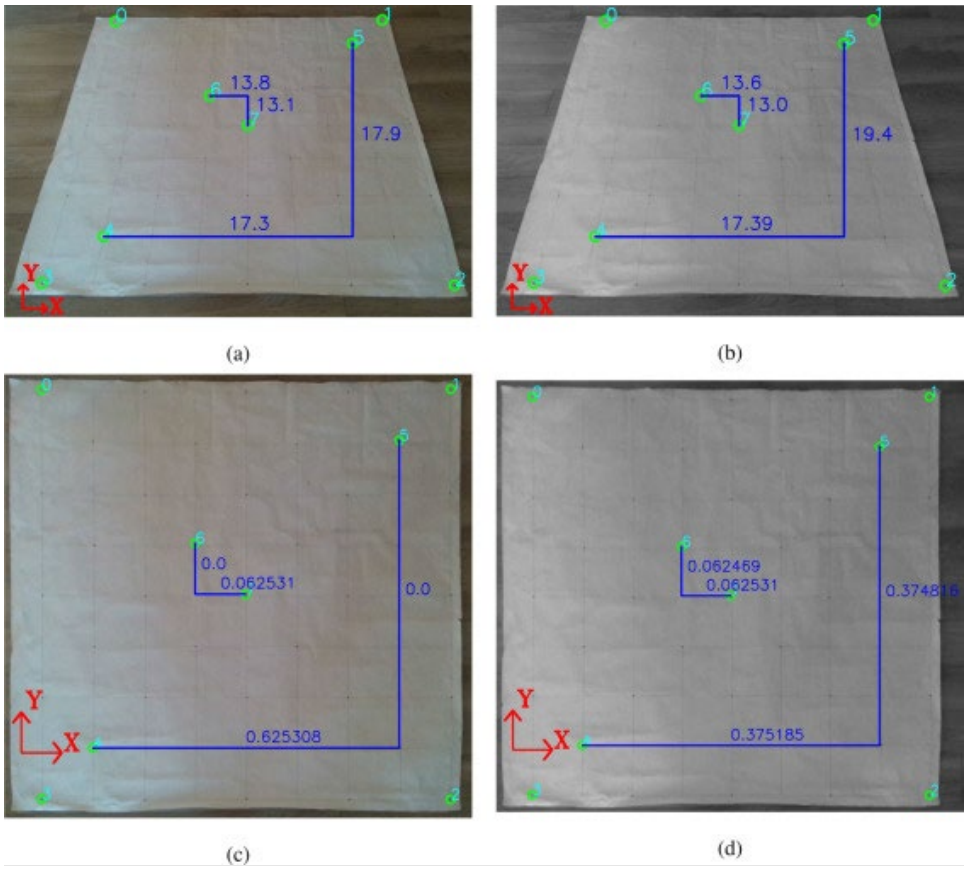

Figure 2.5 Camera calibration results of the RS optical camera (the blue numbers are the error from the calculated distance to the ground truth distance in mm): (a) Original image, (b) Undistorted image corrected in post-processing, (c) Image with only DLT applied, and (d) Image with both distortion correction and DLT applied. (For interpretation of the references to color in this figure legend, the reader is referred to the web version of this article.)

3. EXPERIMENTAL TESTING

In this section, the experimental data sets are introduced. Then preliminary analyses of 2C and 1C measurements are presented, respectively. In the end, a proof of concept test on a cantilever structure is demonstrated.

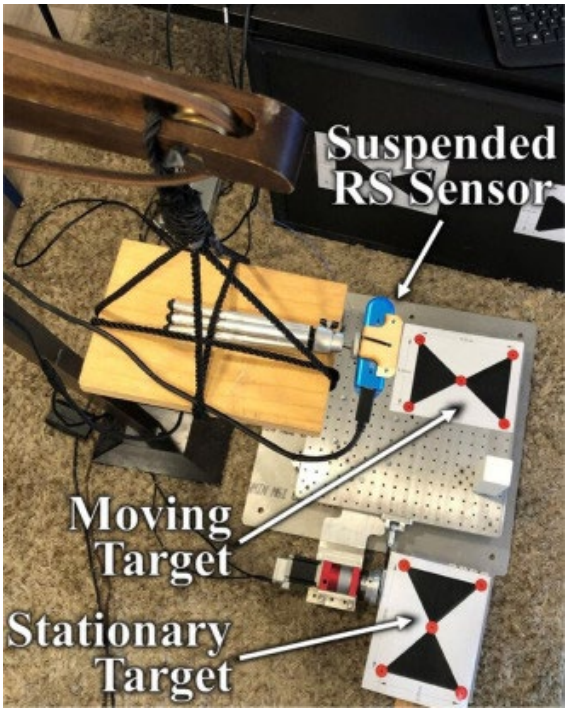

Figure 3.1 Overview of non-stationary 2C planar measurement set-up

3.1 Description of Data Sets

In the experiments, the dynamic displacement of the structure in horizontal directions was produced by a small shaking table with a sine wave input. The signal of the displacement used as the ground truth in the validation was constructed based on the sine wave function (Eq.(5)). The amplitude A was found by manually measuring the diameter of the spinning motor of the shaking table. The frequency, f_0, of the true displacement was found through a Power Spectral Analysis of the accelerometer data using Fast Fourier Transform. Lastly, the phase angle, φ, was determined by minimizing the RMSE between d (Eq.(5)) and results from the measuring techniques tested, as direct data synchronization between the input signal of the shake table and the measurement devices was not an option.

$$d = A \cdot \sin\left(2\pi f_0 \cdot t + \varphi\right) \qquad (5)$$

Based on analysis of the previous study [62], the typical natural frequencies of a variety of civil structures and bridges are between 0.088-Hz (for the world's tallest building, Burj Khalifa, in the United Arab Emirates) to 7.6-Hz (for a 15-m beam bridge), and the average of the reported natural frequencies (without the beam bridges, which have a relatively large natural frequency) is 0.585-Hz[62]. According to the classic Nyquist–Shannon sampling theorem, the sampling frequency must be at least twice the maximum frequency of the vibration to faithfully record the dynamic response. Thus, a sampling frequency greater than 20-Hz is required for monitoring of civil structures. The maximum sampling frequency (e.g., video frame recording rate, or inverse of temporal resolution) for typical low-cost

consumer-level cameras are about 30–90-Hz (fps). So, the requirement in temporal resolution for structural monitoring can be easily achieved using low-cost consumer-level cameras. The input frequencies of the excitation of the shaking table were set at 0.5, 1.0, and 2.0-Hz to test the applicability of the proposed techniques for civil structures. The preliminary 2C and 1C experiments (Section3.2.1 and Section3.2.2, respectively) tests were conducted at a sampling frequency of 30-Hz (or 30-fps), and the maximum frequency of vibration is 2-Hz. The proof-of-concept experiment (Section3.3) was conducted at a sampling frequency of 60-Hz (or 60-fps) and the maximum frequency of vibration was of 4.5-Hz. Therefore, the assigned sampling frequencies (or fps camera recording rate) was sufficient. Note that for applications that require a higher sampling rate, a maximum rate of 90-fps can be achieved with the RS sensor by reducing the resolution of the video.

3.2 Preliminary Experimental Analyses on 2C and 1C Measurements

In this section, small-scale tests were conducted to validate the methodology of the 2C and 1C displacement measurement techniques separately.

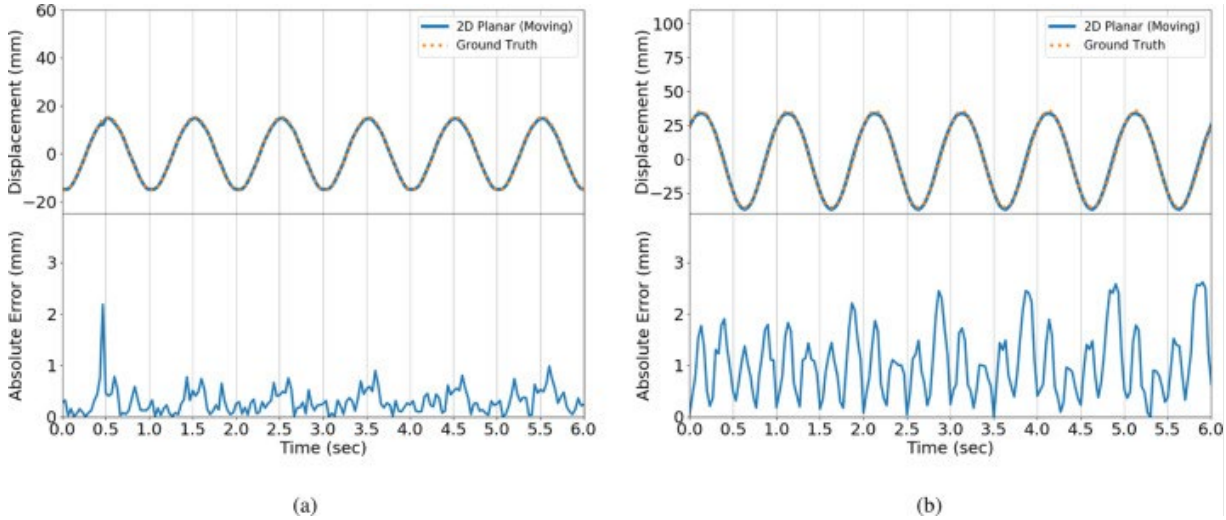

Figure 3.2 Sample displacement measurement results from non-stationary RS optical sensor with time history at top and absolute error at bottom: (a) f_0=1.00-Hz and A = 15.7-mm and (b) f_0=1.00-Hz and A = 35.6-mm.

3.2.1 Analysis of 2C Planar Measurement

First, to ensure accuracy of the 2C planar measurement technique, an accuracy assessment of the camera calibration and DLT was performed on the RS optical sensor. A grid pattern was photographed at an inclined angle, and four measurements of the grid corners were taken. Knowing the dimensions of the grid to be 127-mm on each side, the DLT was applied to transform the image, and the distances on the grid were measured. Figure 2.5a is the original distorted image; the error in millimeters in each direction is labeled on the figure. Figure 2.5b has been corrected for the tangential and radial distortion only and Figure 2.5c has only the DLT applied without correcting the lens distortion. Lastly, Figure 2.5d shows the image that was first corrected for distortion, and then transformed with the DLT (the methodology used within the proposed technique). From the comparison of sub-figures in Figure 2.5, the image with only the DLT applied (Figure 2.5c) has negligible error in the y-direction, but relatively larger error in x-direction. On the other hand, the error from the undistorted and DLT transformed image was consistent in both directions. This remaining error in Figure 2.5d was caused by the small errors in the subpixel location of the four corner reference points, since the DLT used to transform the image was sensitive to

this subpixel location as discussed in Section 2.1. Nevertheless, the measurement accuracy in Figure 2.5d is within a sub-millimeter range with a percent error of less than 0.02%.

With the Camera Calibration and DLT showing minimal error, the efficacy of the proposed 2C planar measurement technique was tested. The RS sensor was suspended above the shaking table and moved slowly (on the order of 0.5-m) to simulate the sensor movement when equipped on a hovering UAV as shown in Figure 3.1 table. A stationary reference target was attached to the ground to track the movement of the RS sensor. The input frequencies of the shaking table were 0.5, 1.0, and 2.0-Hz and the amplitude varied between 15.7-mm and 35.6-mm. The video with the appearance of both the target of interest and ground reference was recorded with 480×640-pixel at 30-fps.

The results of the tests are listed in Table 3.1 with the sample time history of two measurements plotted in Figure 3.2. The RMSE of vibration amplitude is on the order of a couple of millimeters when comparing to the ground truth and consistently small throughout the three input frequencies and two input amplitudes tested. The frequencies of the signals measured by the proposed technique are close to those of the ground truth. The time-varying absolute error shown in Figure 3.2 was caused by randomness of the perspective transformation matrices of the DLT (as the DLT was sensitive to the sub-pixel location of the reference target). Note the results shown are the measurement in *x*-direction. The measurement accuracy in the *y*-direction was similar, while the results were omitted to keep the paper concise.

Table 3.1 Results from 2C non-stationary planar validation test

Ground truth						
Frequency (Hz)	0.495	0.495	1.004	1.004	2.007	2.007
Amplitude (mm)	15.7	35.6	15.7	35.6	15.7	35.6
1C depth measurement						
Number of samples	361	232	186	203	211	255
Total time (s)	12.01	7.70	6.17	6.74	7.00	8.47
Sampling frequency (Hz)	30.06	30.11	30.14	30.13	30.12	30.10
Frequency measured (Hz)	0.501	0.502	0.978	1.040	2.008	2.014
Validation against ground truth						
RMSE (mm)	2.280	2.661	1.353	2.286	2.500	1.553
Mean absolute error (mm)	1.389	2.116	0.699	1.856	1.841	1.318
R2 Score	0.998	0.997	0.998	0.998	0.998	0.995
Error of frequency	1.20%	1.40%	2.62%	3.52%	0.005%	0.35%

3.2.2 Analysis of 1C Depth Measurements

The measurement accuracy of the 1C dynamic displacement using the RS depth sensor placed in a *stationary* position was first tested to lay the foundation for 1C displacement with the *non-stationary* RS sensor equipped on a UAV. The experimental set-up is shown in Figure 3.3. remained the same in this test. The RS sensor was set up perpendicular to the rigid structure at a distance of approximately 0.5-m. The IR image resolution was 1280×720-pixel at 30-fps. The three frequencies of the test found through a Power Spectral Analysis of the time series were compared with those obtained from the accelerometer and the results are listed in Table 3.2, showing an exceptionally good agreement. Additionally, the result of measured time history, absolute error (e.g., the absolute value of the difference between the measured displacement and the ground truth), and power spectral density from two sample tests with different excitation frequencies are shown in Figure 3.4 with a relatively constant level throughout the varying input frequencies. The mean absolute error of vibration amplitude was in the sub-millimeter range. This result suggests that a stationary RS sensor can achieve a high displacement measurement accuracy.

Inherently, with the RS depth sensor, there is measurement noise that increases as the distance from the ROI to the sensor increases. The sensor works best at close range and an experiment was conducted to test noise level and accuracy of the sensor at various distances. In the Realsense SDK 2.0, Intel provides a *Depth Quality Tool* to measure the noise level of each measurement point. By pointing the sensor at a smooth, flat surface, the depth quality tool fits the measured depth points in the ROI to a plane (which gives the mean value of the depth measurements) and calculates the RMSE of the measurements. The result is plotted versus the measurement distance in Figure 3.5

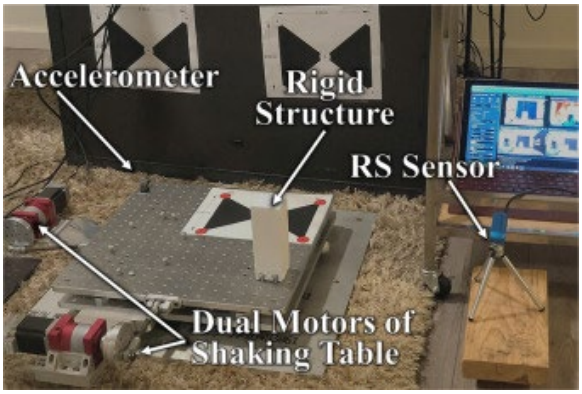

Figure 3.3 Set-up of stationary 1C validation test

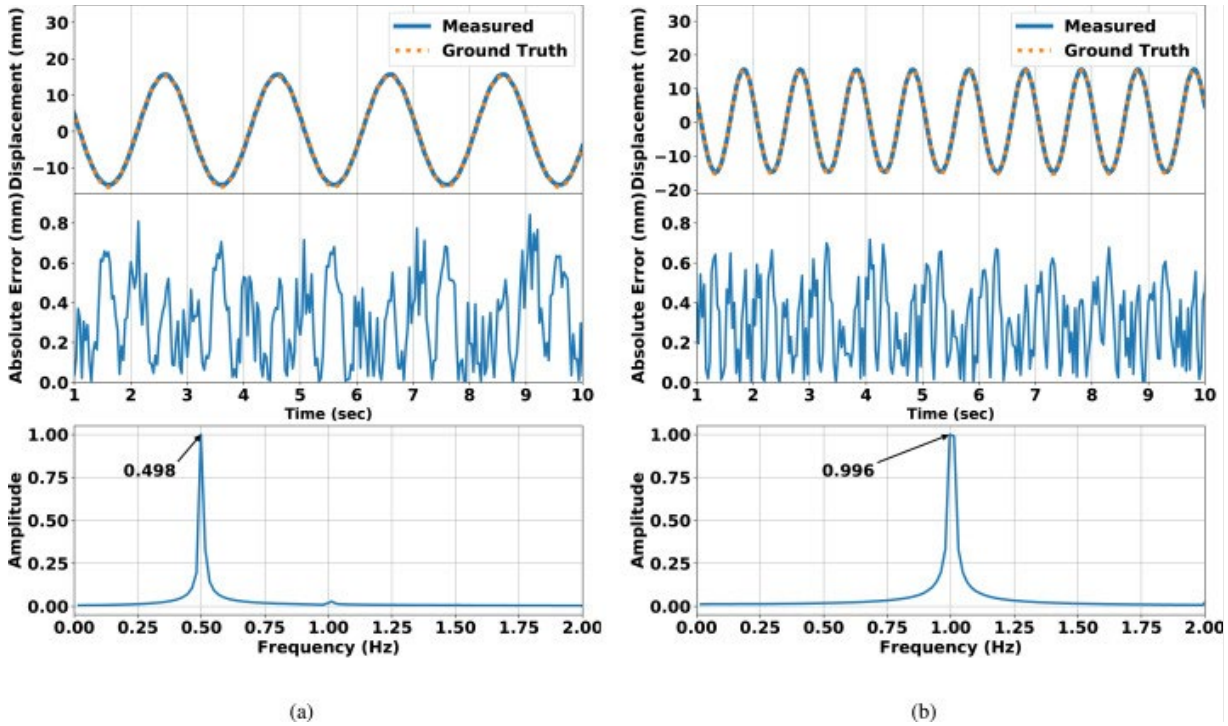

Figure 3.4 Sample displacement measurement results from stationary 1C RS depth sensor with time history at top, absolute error in mm at middle, and power spectral density at bottom: (a) f_0=0.50-Hz and (b) f_0=1.00-Hz.

Table 3.2 Results of stationary 1C RS depth sensor

Ground truth			
Frequency (Hz)	0.495	1.004	2.007
Amplitude (mm)	15.7	15.7	15.7
1C depth measurement			
Number of samples	1749	1749	1749
Total time (s)	58.27	58.27	58.27
Sampling frequency (Hz)	30.07	30.01	30.01
Frequency measured (Hz)	0.498	0.996	2.009
Validation against ground truth			
RMSE (mm)	0.3788	0.3584	0.4243
Mean absolute error (mm)	0.315	0.300	0.356
R^2 Score	0.999	0.999	0.998
Error of frequency	0.402%	0.800%	0.100%

Next, to test the proposed technique using a moving (non-stationary) RS Depth Sensor for structural displacement measurements, the rigid prismatic structure was secured onto the shaking table as before; however, the RS sensor was placed on a rolling cart, which allowed for sensor motion in the depth direction (on the order of 0.5-m) to simulate the drift of the UAV in the *z*-direction. The input frequencies and amplitudes of the shaking table were the same as those for the stationary 1C depth measurement analysis. The IR video with the appearance of both the rigid structure and reference plane was recorded with 480×640-pixel at 30-fps. The results of the tests are listed in Table 3.3 with the sample time histories of two measurements plotted in the RMSE of vibration amplitude is on the order of a few mm and is consistently small throughout the three input frequencies and two input amplitudes tested. The time-varying absolute error shown in Figure3.6 is inherent with the RS depth sensor and its magnitude is a function of the small baseline and α angle (Figure 2.4). The frequencies of the signals measured by the proposed technique agree well with those of the ground truth.

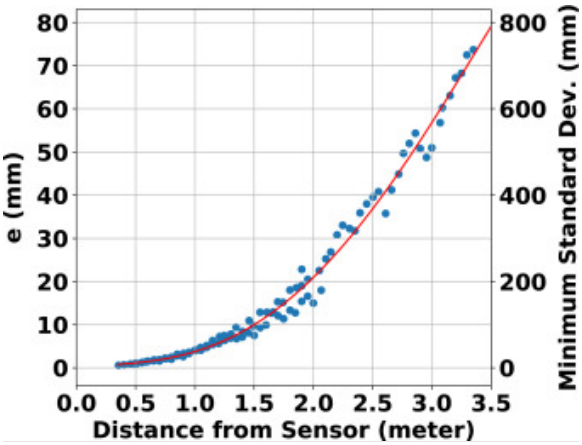

Figure 3.5 Noise floor of the RS depth sensor

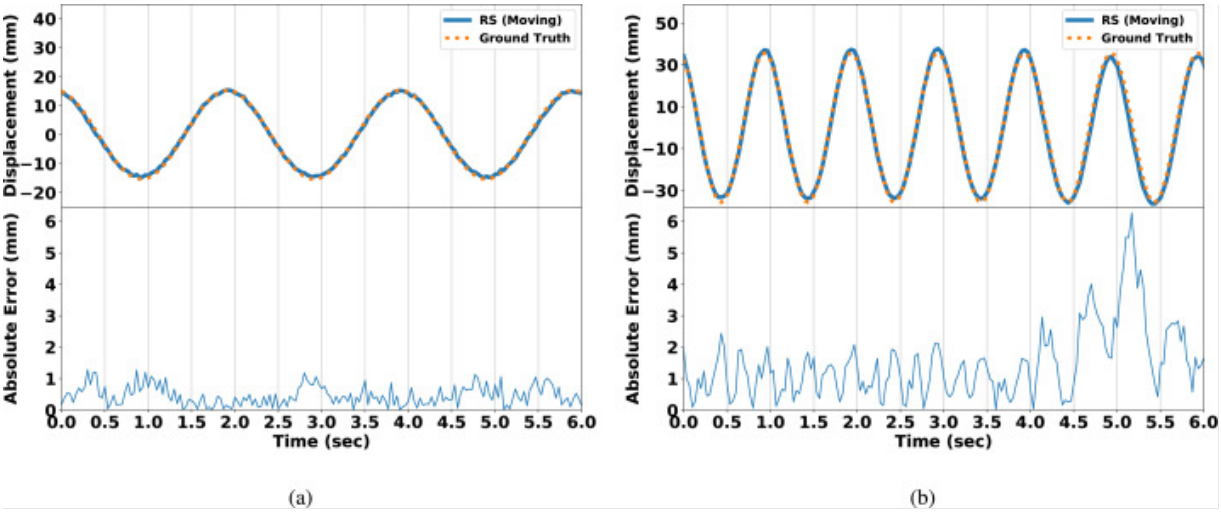

Figure 3.6 Sample displacement measurement results from non-stationary RS depth sensor with time history at Top and absolute error at Bottom: (a) f_0=0.50-Hz and A = 15.7-mm and (b) f_0=1.00-Hz and A = 35.6-mm.

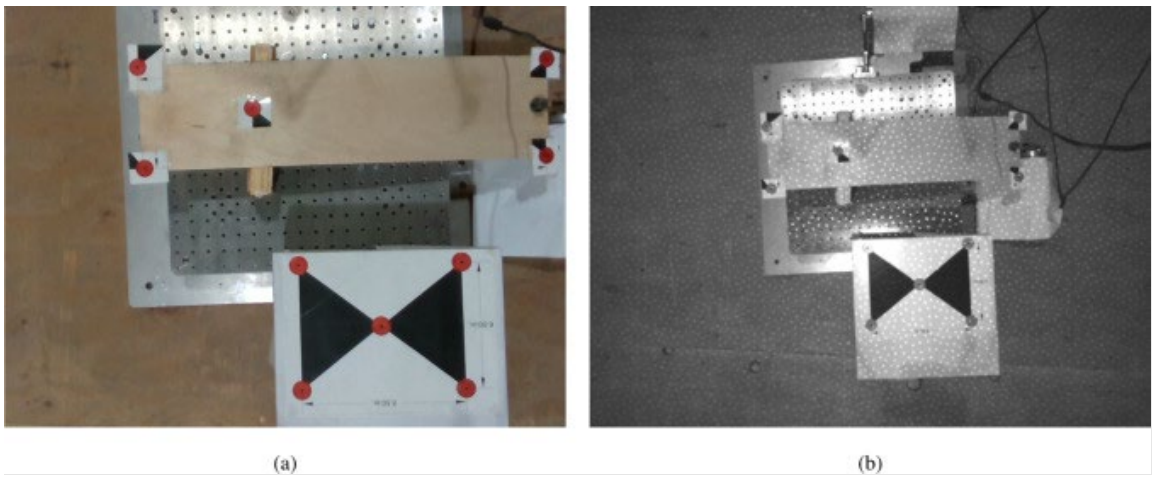

Figure 3.7 POV of RS sensors from 0.75m above ground level: (a) Optical sensor and (b) IR sensor

Table 3.3 Results from 1C non-stationary depth validation test

Ground truth						
Frequency (Hz)	0.495	0.495	1.004	1.004	2.007	2.007
Amplitude (mm)	15.7	35.6	15.7	35.6	15.7	35.6
1C depth measurement						
Number of samples	613	744	693	856	333	673
Total time (s)	20.41	24.82	23.08	29.32	11.07	22.48
Sampling frequency (Hz)	30.03	29.98	30.02	29.20	30.07	29.94
Frequency measured (Hz)	0.491	0.484	0.998	0.990	1.993	2.005
Validation against ground truth						
RMSE (mm)	0.552	2.101	1.068	1.446	0.456	2.855
Mean absolute error (mm)	0.455	1.621	0.907	1.204	0.353	2.229
R2 Score	0.997	0.993	0.990	0.997	0.998	0.985
Error of frequency	0.811%	2.25%	0.599%	1.404%	0.700%	0.100 %

3.3 Proof of Concept: An Experiment on 3C Measurement

This experiment was designed to test the proposed methodology in a small-scale laboratory setting. The double-faceted technique was used to measure the full 3C displacement of the model structure. The UAV was equipped with the RS sensor and optical sensor, and the depth system of the RS sensor was employed to measure the full 3C displacement of the ROI from about 0.75-m above the structure. In the test, a 252.4×609.6-mm cantilever structure constructed of balsa wood was placed on the shaking table with the three-axis accelerometer placed at the end of the cantilever. Reference targets were placed on the cantilever to allow for DLT and a stationary reference target was placed 18-cm from the staking table. The corresponding horizontal measuring distance is 0.735-m for the optical and 1.53-m for the IR image.

Sample images are shown in Figure 3.7. Since the optical sensor has a smaller FOV compared to the IR sensor, the FOV of the optical sensor controlled the height of the UAV in this experiment. The *z*-direction of the structure was excited by flicking the cantilever. Additionally, some small ambient load was generated by the wind induced by the thrust of the UAV's propellers. The shaking table was used to generate the rigid body motion of the structure in *x*- and *y*-directions. In such a way, the displacements in all three directions were produced. The video was recorded at 640×480-pixel at 60-fps. The inputs of the shaking table for this test were 0.5-Hz with an amplitude of 35.6-mm in the *x*-direction and 1.0-Hz with an amplitude of 15.7-mm in the *y*-direction. Given the set-up requirements of the experiment, the flight was performed indoors with a DJI Mavic 2 Pro. This UAV was chosen because of (1) the omnidirectional obstacle avoidance system built into the UAV (including sonar, visible sensors, and a dedicated CPU for stability processing) to ensure a safe flight in the GPS-deprived location and (2) it was extremely stable in-flight with random drifts of about 0.15-m. A DJI Inspire 2 was also tested but proved too unstable in the indoor environment with a significant drift of more than 0.5-m. This greater drift forced the DJI Inspire 2 to fly higher above the cantilever to keep the reference and the ROI in the video, which caused a significant error in the 1C depth measurement due to the increased distance between the camera and the structure. To quickly test the concept of the proposed framework, the RS sensor was wired to a ground control station with a 9-m USB 3.1 cable. The setup for this experiment is shown in Figure 3.8. In a future implementation, the RS sensor could be self-sufficient without the need for the wire when secured to the UAV with an implementation of a micro-controller and a dedicated battery source. Additionally, to provide smoother images, the RS Sensor could be gimballed to the UAV.

The results of the experiment are listed in Table 3.4. The ground truth data for *x*- and *y*-directions were obtained in the same way, as discussed at the beginning of Section 3 and Eq.(5), and are compared in the table. The time histories of the displacements in the *x*- and *y*-directions are shown in Figure 3.9 and the Power Spectral Densities. The results show there was a good agreement between the measured data collected though the proposed double-faceted technique and the ground truth data with a mean absolute error of amplitude less than 2-mm and frequency error less than 0.2% in the *x*- and *y*- directions. For the *z*-direction displacement, transient vibration responses were generated by finger flicking at the tip of the cantilever (Figure 3.10). Due to the transient and non-stationary nature of the response, the time–frequency analysis using continuous Morlet Wavelet Transform was performed to analyze the frequency contents in the signal (Figure 3.10) and identify the natural frequency and damping ratio of the vertical mode[7], [63], [64]. The wavelet skeleton, e.g., wavelet coefficients along the ridge in the wavelet scalogram, were extracted. This skeleton is the analytic signal at the dominant frequency, from which the instantaneous amplitude and phase angles were obtained. By taking the logarithm of the instantaneous amplitude and fitting a linear line for the free decay signal, the damping ratio was obtained (Figure 3.11). The natural frequency was found by fitting a linear line to the phase angle of the wavelet skeleton (Figure 3.11). The instantaneous frequencies and damping ratios for the three transient signals were identified and averaged values are presented in Table 3.5. Since there is no ground truth data for displacement in the *z*-direction, the wavelet scalogram and the natural frequency and damping ratio identified from the displacement data were compared to those obtained by the acceleration measured by the accelerometer. It is seen from Figure 3.10 that the dominant frequency contents from acceleration were slightly higher than those of the displacement, which is expected as the frequency response function (FRF) for acceleration equals the FRF of the displacement multiplied by the frequency squared. The agreement of the natural frequency and damping ratio identified from displacement and those obtained from acceleration is good (Table 3.4), considering the short duration of the signal and inherent larger uncertainties in system identification.

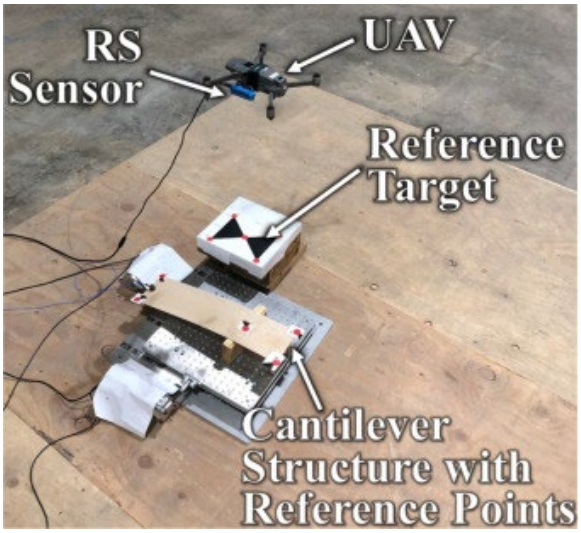

Figure 3.8 Set-up of 3C measurement experiment using a UAV equipped with an RS sensor

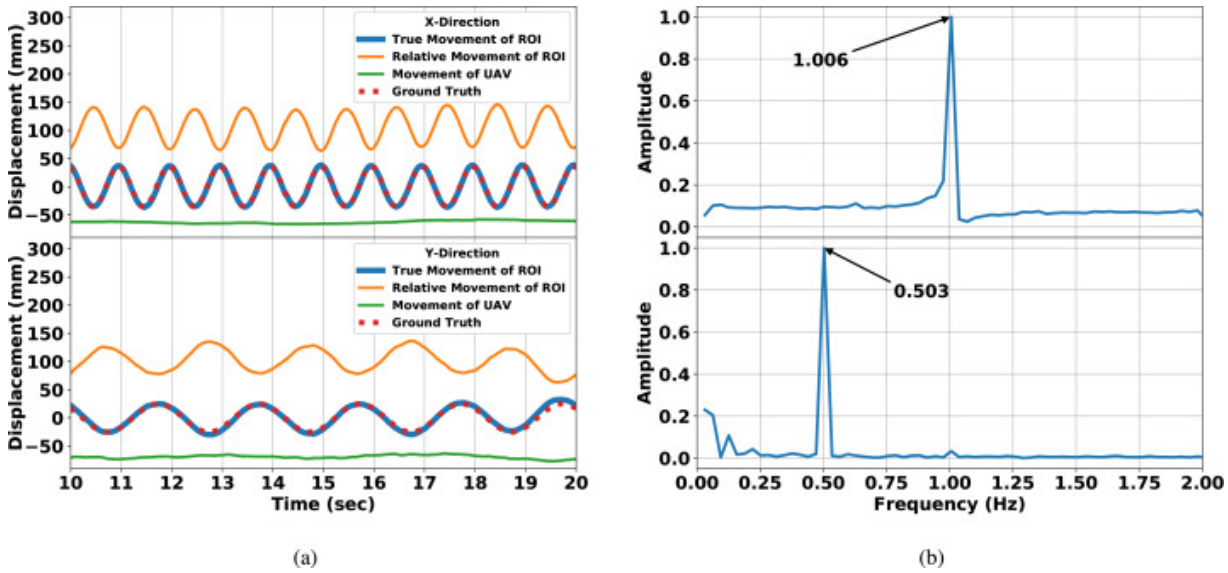

Figure 3.9 Displacement in *x*- and *y*-directions measured by UAV equipped with RS sensor: (a) Time history and (b) Power spectral density.

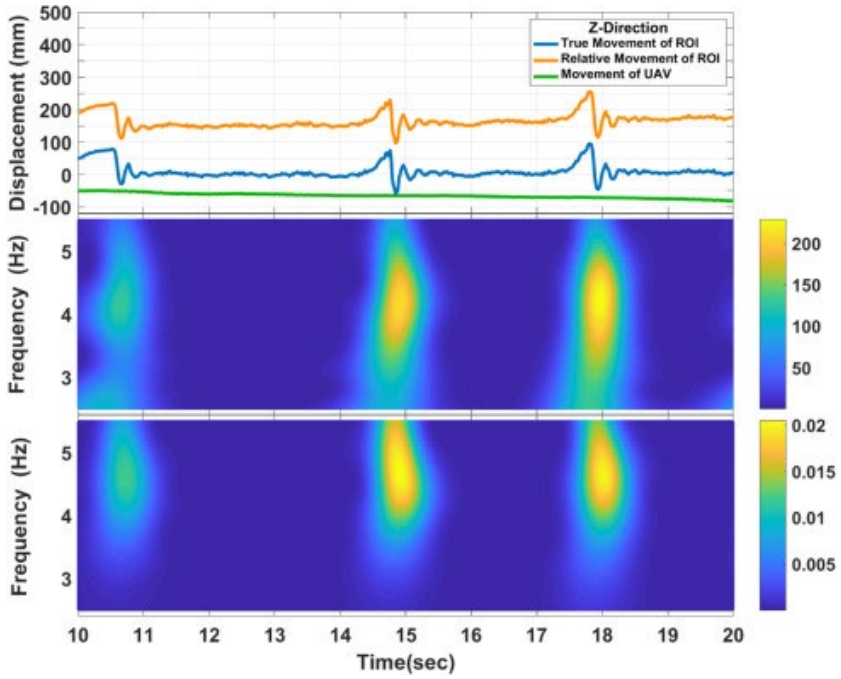

Figure 3.10 Displacement in *z*-direction measured by UAV equipped with an RS sensor with the measured time history at top, the wavelet scalogram of measured displacement at middle, and the wavelet scalogram for acceleration measured by accelerometer at bottom (for Comparison).

Table 3.4 Results from 3C measurement experiment using a UAV equipped with an RS sensor

	X	*Y*	*Z*
Ground Truth			
Frequency (Hz)	0.504	1.007	4.673[a]
Amplitude (mm)	35.6	15.7	-
Damping ratio	-	-	0.0928[a]
Measurement			
Number of sample	1910	1910	1910
Total time (s)	31.83	31.83	31.83
Sampling frequency (Hz)	60.02	60.02	60.02
Frequency measured (Hz)	0.503	1.006	4.431
Damping ratio measured	-	-	0.0970
Validation against ground truth			
RSME (mm)	1.648	3.352	-
Mean absolute score (mm)	1.342	2.514	-
R^2 Score	0.996	0.964	-
Error of frequency	0.199%	0.100%	5.308%
Error of damping ratio	-	-	4.367%

[a]Obtained from Acceleration Using Wavelet Analysis

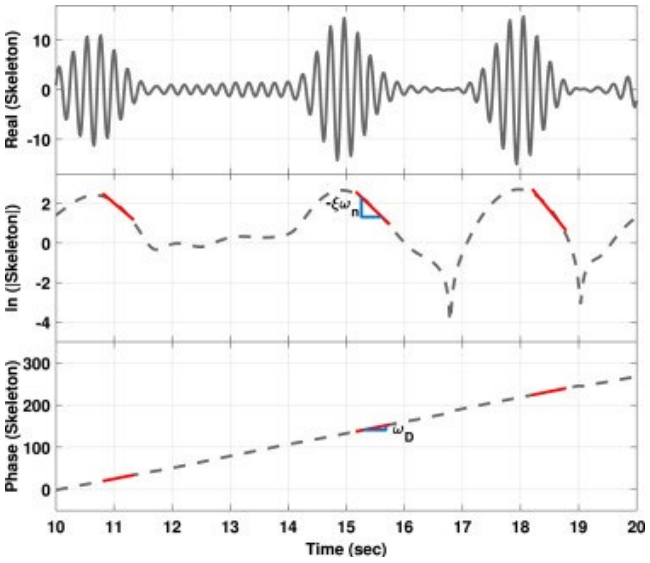

Figure 3.11 Wavelet analysis of *z*-direction displacement

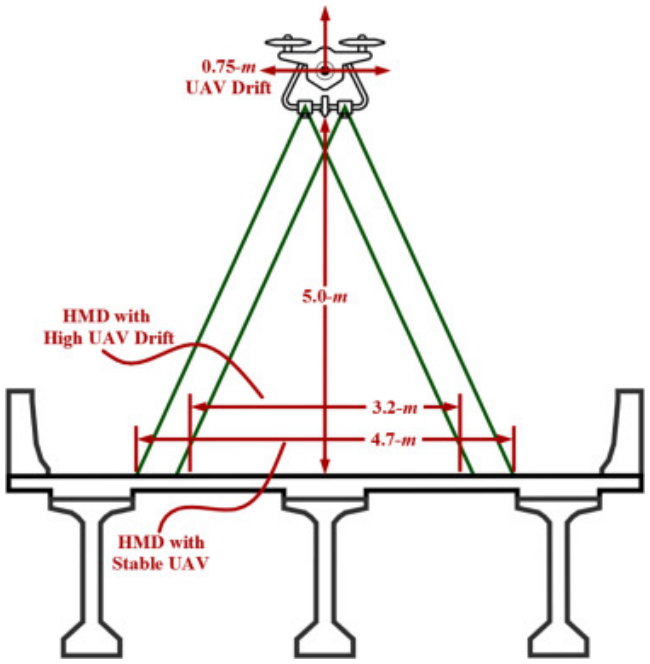

Figure 3.12 Horizontal Measuring Distance (HMD) with *Stable* and *Extreme* drift of a UAV-Enabled flir Grasshopper3 sensor over a scaled two-lane bridge: Baseline = 0.36-m, α = 4.1°, GSD = 0.230-*cm/pix*.

Table 3.5 Comparison of proposed technique to other literature references

Method	*2C planar RMSE*	*2C Freq. error*	*1C depth RMSE*
Proposed			
UAV-enabled 3C Displacement measurement	1.65-mm (4.6%)	0.10%	2.10-mm (5.9%)
Single stationary camera (2C)			
Markers on target locations [20]	-	0.80%	
Markers on target locations [22]	0.5-mm	-	-
LED markers on target locations [28]	-	0.78%	-
Painted speckle pattern [29]	2.7-12.6%	-	-
Stationary stereo vision (3C)			
Markers on target locations [21]	0.52-mm	-	0.35-mm
UAV-enabled single camera (2C)			
High-pass filtering & Adaptive scale factor [42]	-	1.0%	-
High-pass filtering [36]	-	1.6%	-
Feature tracking on background and ROI [41]	2.14-mm	-	-
UAV-based laser doppler vibrometer (1C)			
Vibrometer on UAV [38]	-	-	5%

Table 3.6 Camera configuration for scaling-up the proposed technique

Distance from ROI	0.75-m	5-m	10-m	15-m
IR sensors				
Min. Requirements for 1C depth: α= **4.1°, GSD = 0.240-** cm/pix				
Baseline (m)	0.05	0.36	0.72	1.08
Flir Grasshopper3				
GSD (cm/pix)	**0.070**	**0.230**	0.460	0.690
HMD[a] (m)	1.43	4.71	9.43	14.1
Flir Blackfly S				
GSD (cm/pix)	**0.063**	**0.208**	0.415	0.623
HMD[a] (m)	1.29	4.25	8.50	12.75
Optical Sensors				
Min. Requirements for 2C panar: **GSD = 0.115-** cm/pix				
DJI Zenmuse X7				
GSD (cm/pix)	**0.017**	**0.053**	0.117	0.167
HMD[a] (m)	1.02	3.36	6.71	10.1
DJI Zenmuse X5S				
GSD (cm/pix)	**0.011**	**0.036**	**0.072**	**0.109**
HMD[a] (m)	0.584	1.92	3.84	5.77

[a]Horizontal Measuring Distance (Figure 3.12)

4. DISCUSSION

In this section, the advantages, features, and limitations of the proposed technique are discussed.

1. **Three-component dynamic displacement measurement based on a UAV.** All three components (e.g.,x-, y- and z-directions) of displacement can be measured simultaneously with a UAV-based remote sensing system, which is a superior feature compared to the existing UAV-based displacement measurement techniques that can only measure either two components in a 2D plane[36], [41] or one component in the depth direction[38], [39]. The optical camera and two IR cameras are wire-connected and housed in one unit with electronic synchronization. A high accuracy has been achieved in the laboratory experiments. The maximum frequency and damping estimation errors are 3.5% and 4.4%, respectively. The RMSE for 2C planar displacement is 1.65-mm, while the RMSE for 1C vertical displacement is 2.10-mm (verified in the *non-stationary* depth validation test). In addition, a comparison of the accuracy achieved by the proposed technique (in terms of RMSE) with other related work in the literature is presented in Table 3.5. The level of the measurement accuracy achieved by the proposed technique proves sufficient for SHM application to civil structures[4].

2. **Portable sensing.** This technique eliminates the need for attaching contact sensors (wired and/or wireless) to a structure and gives the capability of moving measurement locations quickly and easily. The UAV platform allows the sensors to hover adjacent to a structure from a desired angle, facilitating high-quality data collection. This is a major advantage compared to other non-contact sensing techniques based on stationary cameras or laser Doppler vibrometers[20], [21], [22], [23], [24], [25], [26], [27], [28], [29], [30], whose use might be limited by not being able to find an appropriate sensor placement location in field. These nice features regarding portable sensing are also reported in other UAV-based dynamic displacement measurement studies in the literature[36], [37], [38], [39], [40], [41], [42].

3. **Full-field measurement.** The proposed technique allows measuring the response over the entire FOV of the sensors with a single sensor suite instead of the point-based conventional measurements in other approaches that may require instrumentation of multiple sensors, such as GPS, accelerometer, laser sensing, etc. The advantage of full-field measurements has also been reported in other camera-based displacement measurement studies[37], [40].

4. **Computational time.** Fast data processing and computational efficiency were achieved. In one epoch (or iteration of a frame in the video), it took about 0.071-s to extract the targets, track their movements, and take the measurements for both the ROIs and stationary references. As an example, a measurement sample with time length of five minutes and a video recording rate at 30-fps, the data processing time was 11-minutes.

5. **Length of monitoring time.** The proposed approach provides a portable alternative for short-term monitoring or modal testing. The minimum data length required for the identification of the dynamic properties in modal testing is about 5–30 minutes [5] for most civil structures, depending on the natural frequencies of the structure. The maximum length of continuous monitoring time is determined by the battery life of a UAV. For instance, the Mavic Pro has a flight time of about 25-minutes with the added payload required in this study. Some UAV platforms have a longer flight time (e.g., 45-minutes for DJI 300 RTK with the required payload). Therefore, the typical consumer-level UAVs can satisfy the time length requirement in short-term monitoring or modal testing. The dynamic properties can be measured multiple times over a long term to help identify potential changes in the condition of a structure though various data-driven approaches[8], [9], [10], [11], [12].

6. Considerations to scale-up the technique for field application:

(a) Measurement accuracy. To apply this technique to field application, a longer working distance between the UAV and the structure is desired. To achieve a similar level of accuracy, the GSD of both the IR and optical sensors must be similar or better and the angle between the two IR cameras, α, (Figure 2.4a) should be equal to or greater than in the current experiments. This requires using cameras with higher resolution and longer baseline (Figure 3.4a), and a laser projector with a longer working distance. Table 3.6 examines several higher resolution commercial-level sensors and the required baseline that can potentially work for a longer distance. The bold numbers show GSD similar to or less than that in the current study. From this table, 5-m is about the longest working distance for the considered sensors to produce a similar accuracy as the proof of concept test (controlled by the GSD of the IR cameras). The longer baseline (0.36-m) also requires a larger UAV platform (e.g., DJI Matrice 600 Pro or DJI Matrice 300 RTK). The corresponding measurement field (e.g., HMD in Table 3.7) is relatively small at 5-m, which would not allow for full-structure monitoring for most civil structures; however, multiple flights could be performed in 5-m intervals to survey the entire structure.

(b) Reference target size and location. The size of the reference target is dependent on the GSD of the optical camera. In this proof of concept, the diameter of the red targets was 2.54-cm. If the GSD of the optical camera is similar to the proof of concept test, a similarly sized reference target could be used. In the laboratory experiments, the reference target was located close to the structure, so it was in the same image frame as the ROI. In large-scale applications, it might not be feasible to have the reference and structure in the same frame due to the constraints of the measurement field of the cameras (e.g., the HMD in Table 3.7). This issue is also shown in Figure 3.12, where the HMDs of IR sensors (Flir Grasshopper 3) with a stable UAV flight and 0.75-m UAV drift are both presented with respect to a two-lane bridge. In this case, there are three possible solutions. (1) One may use additional cameras to track the reference target, which may be put beside or under a structure (e.g., bridge), depending on the field condition. (2) Using higher-end sensors and a larger UAV platform allows a longer working distance to increase the measuring field (HMD); the reference target can then be placed beside the structure. (3) The reference target can be omitted, and the UAV motion will be removed in post-processing using a digital filter. The feasibility of this approach has been reported in[36], [42].

(c) Lighting condition. The virtual speckle pattern projected by the IR projector is less visible in direct sunlight. However, the proposed technique can be used in the shadowed areas (e.g., under a bridge or on the shaded side of a building) or after sunset. The current bridge inspection may occur during the nighttime to alleviate the traffic interruptions, which provides a more favorable lighting condition for the application of the proposed technique.

(d) **Wind conditions.** UAV platforms can fly under moderate wind condition (15-m/s for the DJI Matrice 300 RTK and 8-m/s for the DJI Matrice 600 Pro). So, the proposed technique cannot be applied during high winds.

(e) **UAV Operations.** It is recommended to have a three-person team to conduct the survey. One as a pilot (in the United States, a certified pilot must operate the UAV), one as a visual observer to ensure a safe flight, and one to manage data acquisition.

(f) **Occlusions.** One issue of monitoring real-world structures is occlusions from trees or other debris close to the structure. This would require careful pre-flight planning and possible vegetation mitigation.

7. **Cost-effectiveness.** High accuracy was achieved with an affordable sensor and UAV, demonstrating an attractive cost-effectiveness benefit for small-scale applications. For large-scale field applications, a larger UAV platform would be needed to support a larger baseline between the two IR cameras (such as the DJI Matrice 600 Pro or DJI Matrice 300 RTK). Additionally, the three cameras (one optical and two IR sensors) would need to have better quality, and a microprocessor would need to be mounted on the UAV to allow for local data storage. A price comparison of some possible configurations (based on the examined sensors in Table 3.7) is shown in Table 4.1. This level of equipment is quite common in state DOT's applications [65] in the United States, showing the feasibility of the technology adoption.

Table 4.1 Price estimations (prices in USD)

	UAVs			Optical Sensors		IR Sensors		
	DJI	DJI	DJI	DJI	DJI	Flir	Flir	
Configurations	Mavic 2 Pro w/ RS Sensor **($1,778)**	Matrice 300 RTK **($10,599)**	Matrice 600 Pro **($6,599)**	X7 **($2,899)**	X5S **($2,348)**	Grass-hopper3 **($1,529**	Blackfly S **($1,230)**	Total
Tested	X							$1,778
Best		X		X		X		$16,556
Cheapest			X		X		X	$11,407

5. CONCLUDING REMARKS

In this section, the advantages, features, and limitations of the proposed technique are discussed. This paper proposes a new 3C displacement measurement technique. A new sensing system with an integrated optical sensor, two IR sensors, and an IR projector on a UAV platform was proposed. 3C measurements were achieved by simultaneously capturing the 2C planar motion by an optical camera and 1C depth motion using IR cameras. Based on target identification, DLT, and active stereo vision, a double-faceted computer vision-based algorithm was developed to extract the 3C dynamic displacement of structures from the videos. The high accuracy and cost-effectiveness of the technique have been proved in a small-scale laboratory setting through comprehensive experimental testing. This study contributed to advancing the UAV-based portable sensing techniques for dynamic displacement measurement by enabling simultaneous measurements of all three components, as opposed to only 2C or 1C in existing UAV-based remote-sensing studies. The considerations for scaling-up the technique in field application were discussed.

REFERENCES

[1] Z. Li, C.C. Chang, Tracking of structural dynamic characteristics using recursive stochastic subspace identification and instrumental variable technique, J. Eng. Mech. 138 (6) (2012) 591–600, http://dx.doi.org/10.1061/(ASCE)EM.1943- 7889.0000370.

[2] C. Rainieri, G. Fabbrocino, Automated output-only dynamic identification of civil engineering structures, Mech. Syst. Signal Process. 24 (3) (2010) 678–695, http://dx.doi.org/10.1016/j.ymssp.2009.10.003.

[3] R. Brincker, L. Zhang, P. Andersen, Modal identification from ambient responses using frequency domain decomposition, in: IMAC 18: Proceedings of the International Modal Analysis Conference, San Antonio, TX, 2000, pp. 625–630.

[4] Y. Guo, A. Kareem, Y. Ni, W. Liao, Performance evaluation of Canton Tower under winds based on full-scale data, J. Wind Eng. Ind. Aerodyn. 104–106 (2012) 116–128, http://dx.doi.org/10.1016/j.jweia.2012.04.001.

[5] Y. Guo, A. Kareem, Non-stationary frequency domain system identification using time–frequency representations, Mech. Syst. Signal Process. 72–73 (2016) 712–726, http://dx.doi.org/10.1016/j.ymssp.2015.10.031.

[6] Y. Guo, A. Kareem, System identification through nonstationary data using time–frequency blind source separation, J. Sound Vib. 371 (2016) 110–131, http://dx.doi.org/10.1016/j.jsv.2016.02.011.

[7] Y. Guo, A. Kareem, System identification through nonstationary response: wavelet and transformed singular value decomposition–based approach, J. Eng. Mech. 141 (7) (2015) 04015013, http://dx.doi.org/10.1061/(ASCE)EM.1943- 7889.0000905.

[8] X. Ma, Y. Lin, Z. Nie, H. Ma, Structural damage identification based on unsupervised feature-extraction via variational auto-encoder, Measurement 160 (2020) 107811, http://dx.doi.org/10.1016/j.measurement.2020.107811.

[9] Y.Q. Ni, X.G. Hua, K.Y. Wong, J.M. Ko, Assessment of bridge expansion joints using long-term displacement and temperature measurement, J. Perform. Constr. Facil. 21 (2) (2007) 143–151, http://dx.doi.org/10.1061/(ASCE)0887-3828(2007)21:2(143).

[10] X.W. Ye, T. Jin, C.B. Yun, A review on deep learning-based structural health monitoring of civil infrastructures, Smart Struct. Syst. 24 (5) (2019) 567–586, http://dx.doi.org/10.12989/sss.2019.24.5.567.

[11] X.W. Ye, C.Z. Dong, T. Liu, A review of machine vision-based structural health monitoring: methodologies and applications, J. Sensors 2016 (2016) 1–10, 7103039, http://dx.doi.org/10.1155/2016/7103039.

[12] T. Teimoori, M. Mahmoudi, Damage detection in connections of steel moment resisting frames using proper orthogonal decomposition and wavelet transform, Measurement 166 (2020) 108188, http://dx.doi.org/10.1016/j.measurement. 2020.108188.

[13] H. Sekiya, K. Kimura, C. Miki, Technique for determining bridge displacement response using MEMS accelerometers, Sensors 16 (2) (2016) 257, http://dx.doi.org/10.3390/s16020257.

[14] F. Moschas, S. Stiros, Measurement of the dynamic displacements and of the modal frequencies of a short-span pedestrian bridge using GPS and an accelerometer, Eng. Struct. 33 (1) (2011) 10–17, http://dx.doi.org/10.1016/j. engstruct.2010.09.013.

[15] G.W. Roberts, X. Meng, A.H. Dodson, Integrating a global positioning system and accelerometers to monitor the deflection of bridges, J. Surv. Eng. 130 (2) (2004) 65–72, http://dx.doi.org/10.1061/(ASCE)0733-9453(2004)130:2(65).

[16] M.R. Kaloop, J.W. Hu, Stayed-cable bridge damage detection and localization based on accelerometer health monitoring measurements, Shock Vib. 2015 (2015) 1–11, 102680, http://dx.doi.org/10.1155/2015/102680.

[17] R.J. Brown, K.O. Gaebler, C.K. Shield, L.E. Linderman, Displacement Monitoring of I-35W Saint Anthony Falls Bridge with Current Vibration-Based System, Tech. Rep. MN/RC 2019-05, Minnesota Department of Transportation, Minneapolis, MN, 2019, URL http://www.dot.state.mn.us/research/reports/2019/201905.pdf.

[18] T. Kijewski-Correa, A. Kareem, Y. Guo, R. Bashor, T. Weigand, Performance of tall buildings in urban zones: lessons learned from a decade of full-scale monitoring, Int. J. High-Rise Build. 2 (3) (2013) 179–192, http://dx.doi.org/10.21022/IJHRB.2013.2.3.179.

[19] T. Kijewski-Correa, A. Kareem, M. Kochly, Experimental verification and fullscale deployment of global positioning systems to monitor the dynamic response of tall buildings, J. Struct. Eng. 132 (8) (2006) 1242–1253, http://dx.doi.org/10.1061/(ASCE)0733-9445(2006)132:8(1242).

[20] A. Havaran, M. Mahmoudi, Extracting structural dynamic properties utilizing close photogrammetry method, Measurement 150 (2020) 107092, http://dx.doi.org/10.1016/j.measurement.2019.107092.

[21] X. Liu, X. Tong, W. Lu, S. Liu, B. Huang, P. Tang, T. Guo, High-speed videogrammetric measurement of the deformation of shaking table multilayer structures, Measurement 154 (2020) 107486, http://dx.doi.org/10.1016/j.measurement.2020.107486.

[22] L.-J. Wu, F. Casciati, S. Casciati, Dynamic testing of a laboratory model via vision-based sensing, Eng. Struct. 60 (2) (2014) 113–125, http://dx.doi.org/10.1016/j.engstruct.2013.12.002.

[23] X. Ye, Y. Ni, T. Wai, K. Wong, X. Zhang, F. Xu, A vision-based system for dynamic displacement measurement of long-span bridges: algorithm and verification, Smart Struct. Syst. 12 (3) (2013) 363–379, http://dx.doi.org/10.12989/sss.2013.12.3_4.363.

[24] X. Ye, T.-H. Yi, C. Dong, T. Liu, Vision-based structural displacement measurement: system performance evaluation and influence factor analysis, Measurement 88 (2016) 372–384, http://dx.doi.org/10.1016/j.measurement.2016.01.024.

[25] X. Ye, C. Dong, T. Liu, Image-based structural dynamic displacement measurement using different multi-object tracking algorithms, Smart Struct. Syst. 17 (6) (2016) 935–956, http://dx.doi.org/10.12989/sss.2016.17.6.935.

[26] X. Ye, C. Dong, T. Liu, Force monitoring of steel cables using vision-based sensing technology: methodology and experimental verification, Smart Struct. Syst. 18(3) (2016) 585–599, http://dx.doi.org/10.12989/sss.2016.18.3.585.

[27] X. Ye, T.-H. Yi, C. Dong, T. Liu, H. Bai, Multi-point displacement monitoring of bridges using a vision-based approach, Wind Struct. 20 (2) (2015) 315–326, http://dx.doi.org/10.12989/was.2015.20.2.315.

[28] C. Dong, X. Ye, T. Jin, Identification of structural dynamic characteristics based on machine vision technology, Measurement 126 (2018) 405–416, http://dx.doi.Org/10.1016/j.measurement.2017.09.043.

[29] R. Aghlara, M.M. Tahir, Measurement of strain on concrete using an ordinary digital camera, Measurement 126 (2018) 398–404, http://dx.doi.org/10.1016/j.measurement.2018.05.066.

[30] G. Almeida, H. Biscaia, C. Chastre, J. Fonseca, F. Melício, Displacement estimation

of a RC beam test based on TSS algorithm, in: Proceedings of the 5th Iberian Conference on Information Systems and Technologies, CISTI 2010, IEEE, Santiago de Compostela, Spain, 2010, pp. 1–4.

[31] B. Gencturk, K. Hossain, A. Kapadia, E. Labib, Y.-L. Mo, Use of digital image correlation technique in full-scale testing of prestressed concrete structures, Measurement 47 (2014) 505–515, http://dx.doi.org/10.1016/j.measurement.2013.09.018.

[32] M.N. Gillins, D.T. Gillins, C. Parrish, Cost-effective bridge safety inspections using unmanned aircraft systems (UAS), in: Geotechnical and Structural Engineering Congress 2016, ASCE, Reston, VA, 2016, pp. 1931–1940, http://dx.doi.org/10.1061/9780784479742.165.

[33] J. Wells, B. Lovelace, Improving the Quality of Bridge Inspections Using Unmanned Aircraft Systems (UAS), Tech. Rep. MN/RC 2018-26, Minnesota Department of Transportation, St. Paul, MN, 2018, URL http://www.dot.state.mn.us/research/reports/2018/201826.pdf.

[34] B.J. Perry, Y. Guo, R. Atadero, J.W. van de Lindt, Streamlined bridge inspection system utilizing unmanned aerial vehicles (UAVs) and machine learning, Measurement 164 (2020) 108048, http://dx.doi.org/10.1016/j.measurement.2020.108048.

[35] Y. Xu, Y. Turkan, BrIM and UAS for bridge inspections and management, Eng. Construct. Archit. Manage. 27 (3) (2019) 785–807, http://dx.doi.org/10.1108/ECAM-12-2018-0556.

[36] V. Hoskere, J.W. Park, H. Yoon, B.F. Spencer, Vision-based modal survey of civil infrastructure using unmanned aerial vehicles, J. Struct. Eng. 145 (7) (2019) 04019062, http://dx.doi.org/10.1061/(ASCE)ST.1943-541X.0002321.

[37] M. Kalaitzakis, S.R. Kattil, N. Vitzilaios, D. Rizos, M. Sutton, Dynamic structural health monitoring using a DIC-enabled drone, in: 2019 International Conference on Unmanned Aircraft Systems (ICUAS), IEEE Xplore, Atlanta, GA, 2019, pp. 321–327, http://dx.doi.org/10.1109/ICUAS.2019.8798270.

[38] P. Garg, F. Moreu, A. Ozdagli, M.R. Taha, D. Mascareñas, Noncontact dynamic displacement measurement of structures using a moving laser doppler vibrometer, J. Bridge Eng. 24 (9) (2019) 04019089, http://dx.doi.org/10.1061/(ASCE) BE.1943-5592.0001472.

[39] P. Garg, R. Nasimi, A. Ozdagli, S. Zhang, D.D.L. Mascarenas, M. Reda Taha, F. Moreu, Measuring transverse displacements using unmanned aerial systems laser doppler vibrometer (UAS-LDV): development and field validation, Sensors 20 (21) (2020) 6051, http://dx.doi.org/10.3390/s20216051.

[40] S. Catt, B. Fick, M. Hoskins, J. Praski, J. Baquersad, Development of a semiautonomous

drone for structural health monitoring of structures using digital image correlation (DIC), in: Structural Health Monitoring, Photogrammetry &DIC Volume 6. Conference Proceedings of the Society for Experimental Mechanics Series, Springer International Publishing, Greenville, SC, 2019, pp. 49–57, http://dx.doi.org/10.1007/978-3-319-74476-6_7.

[41] H. Yoon, J. Shin, B.F. Spencer, Structural displacement measurement using an unmanned aerial system, Comput.-Aided Civ. Infrastruct. Eng. 33 (3) (2018) 183–192, http://dx.doi.org/10.1111/mice.12338.

[42] H. Yoon, V. Hoskere, J.-W. Park, B.F. Spencer Jr., Cross-correlation-based structural system identification using unmanned aerial vehicles, Sensors 17 (9) (2017) 1–12, 2075, http://dx.doi.org/10.3390/s17092075.

[43] H. Fathi, I. Brilakis, Automated sparse 3D point cloud generation of infrastructure using its distinctive visual features, Adv. Eng. Inform. 25 (4) (2011) 760–770, http://dx.doi.org/10.1016/j.aei.2011.06.001.

[44] K. Konolige, Projected texture stereo, in: 2010 IEEE International Conference on Robotics and Automation, IEEE, Anchorage, AK, 2010, pp. 148–155, http://dx.doi.org/10.1109/ROBOT.2010.5509796.

[45] Y. Shuang, Z. Wang, Active stereo vision three-dimensional reconstruction by RGB dot pattern projection and ray intersection, Measurement 167 (2021) 108195, http://dx.doi.org/10.1016/j.measurement.2020.108195.

[46] D. Beltran, L. Basañez, A comparison between active and passive 3D vision sensors: BumblebeeXB3 and Microsoft Kinect, in: Advances in Intelligent Systems and Computing, Vol. 252, Springer International Publishing, Cham, 2014, pp.725–734, http://dx.doi.org/10.1007/978-3-319-03413-3_54.

[47] A.J. Cawood, C.E. Bond, J.A. Howell, R.W. Butler, Y. Totake, LiDAR, UAV or compass-clinometer? Accuracy, coverage and the effects on structural models, J. Struct. Geol. 98 (2017) 67–82, http://dx.doi.org/10.1016/j.jsg.2017.04.004.

[48] N. Torres, F.R. Ortega, J. Bernal, A. Barreto, N.D. Rishe, Towards multi-modal interaction with interactive paint, in: 12th International Conference, Universal Access in Human-Computer Interaction 2018, Held As Part of Human-Computer Interaction International 2018, Springer International Publishing, Las Vegas, NV, 2018, pp. 299–308, http://dx.doi.org/10.1007/978-3-319-92049-8_22.

[49] H. Aoki, A. Suzuki, T. Shiga, Study on non-contact heart beat measurement method by using depth sensor, in: World Congress on Medical Physics and Biomedical Engineering 2018, Springer, Prague, Czech Republic, 2019, pp. 341–345, http://dx.doi.org/10.1007/978-981-10-9035-6_62.

[50] M. Barzegar, G.P. Redding, C.E. Davies, L. Fullard, M.C. Grafton, Measurement of fill volume of a storage vessel by optical means, in: 13th International Conference on Bulk Materials Storage, Handling & Transportation, Engineers Australia, Surfers Paradise, Australia, 2019, pp. 835–842.

[51] R. Tsai, A versatile camera calibration technique for high-accuracy 3D machine vision metrology using off-the-shelf TV cameras and lenses, IEEE J. Robot. Autom. 3 (4) (1987) 323–344, http://dx.doi.org/10.1109/JRA.1987.1087109.

[52] Z. Zhang, A flexible new technique for camera calibration, IEEE Trans. Pattern Anal. Mach. Intell. 22 (11) (2000) 1330–1334, http://dx.doi.org/10.1109/34. 888718.

[53] J. Weng, P. Cohen, M. Herniou, Camera calibration with distortion models and accuracy evaluation, IEEE Trans. Pattern Anal. Mach. Intell. 14 (10) (1992) 965–980, http://dx.doi.org/10.1109/34.159901.

[54] Z. Zhang, Flexible camera calibration by viewing a plane from unknown orientations, in: Proceedings of the Seventh IEEE International Conference on Computer Vision, Vol. 1, IEEE, Kerkyro, Greece, 1999, pp. 666–673, http://dx.doi.org/10.1109/ICCV.1999.791289.

[55] J. Heikkila, O. Silven, A four-step camera calibration procedure with implicit image correction, in: Proceedings of IEEE Computer Society Conference on Computer Vision and Pattern Recognition, IEEE Comput. Soc, San Juan, PR, 1997, pp. 1106–1112, http://dx.doi.org/10.1109/CVPR.1997.609468.

[56] J.-Y. Bouguet, Camera calibration toolbox for Matlab, 2015, URL http://www.vision.caltech.edu/bouguetj/calib_doc/index.html.

[57] M. Adamczyk, P. Liberadzki, R. Sitnik, Temperature compensation method for digital cameras in 2D and 3D measurement applications, Sensors 18 (11) (2018)3685, http://dx.doi.org/10.3390/s18113685.

[58] S. Suzuki, K. Be, Topological structural analysis of digitized binary images by border following, Comput. Vis. Graph. Image Process. 30 (1) (1985) 32–46, http://dx.doi.org/10.1016/0734-189X(85)90016-7.

[59] D. Bolme, J.R. Beveridge, B.A. Draper, Y.M. Lui, Visual object tracking using adaptive correlation filters, in: 2010 IEEE Computer Society Conference on Computer Vision and Pattern Recognition, IEEE, San Francisco, CA, 2010, pp.2544–2550, http://dx.doi.org/10.1109/CVPR.2010.5539960.

[60] A. Lukežič, T. Vojíř, L. Čehovin Zajc, J. Matas, M. Kristan, Discriminative correlation filter tracker with channel and spatial reliability, Int. J. Comput. Vis. 126 (7) (2018) 671–688, http://dx.doi.org/10.1007/s11263-017-1061-3.

[61] Y. Wang, W. Shi, S. Wu, Robust UAV-based tracking using hybrid classifiers, Mach. Vis. Appl. 30 (1) (2019) 125–137, http://dx.doi.org/10.1007/s00138-018-0981-4.

[62] G. Morgenthal, H. Höpfner, The application of smartphones to measuring transient structural displacements, J. Civ. Struct. Health Monit. 2 (3) (2012)149–161, http://dx.doi.org/10.1007/s13349-012-0025-0.

[63] T. Kijewski, A. Kareem, Wavelet transforms for system identification in civil engineering, Comput.-Aided Civ. Infrastruct. Eng. 18 (5) (2003) 339–355, http://dx.doi.org/10.1111/1467-8667.t01-1-00312.

[64] Y. Guo, D.K. Kwon, A. Kareem, Near-real-time hybrid system identification framework for civil structures with application to Burj Khalifa, J. Struct. Eng. 142(2) (2016) 04015132, http://dx.doi.org/10.1061/(ASCE)ST.1943-541X.0001402.

[65] S. Pandey, M. Haider, N. Uddin, Design and implementation of a low-cost wireless platform for remote bridge health monitoring, Int. J. Emerg. Technol. Adv. Eng. 6 (6) (2016) 57–62.